Materials Advances

ROYAL SOCIETY OF CHEMISTRY

PAPER

View Article Online
View Journal | View Issue

Cite this: *Mater. Adv.*, 2025, 6, 3596

GSAG:Ce scintillator: material optimization and intrinsic bottlenecks†

M. Nikl, *[a] J. Pejchal, [a] J. Ježek, [b] D. Sedmidubský,[b] V. Laguta, [a] V. Babin, [a] A. Beitlerová[a] and R. Kučerková[a]

Received 3rd February 2025,
Accepted 12th May 2025

DOI: 10.1039/d5ma00095e

rsc.li/materials-advances

Several Sc-admixed garnet single crystals of the general composition $(Gd,Sc)_3(Sc,Al)_5O_{12}$:Ce and the well-established $Gd_3Ga_{2.7}Al_{2.3}O_{12}$:Ce (GGAG:Ce) one were grown using the micropulling down method. Their optical, luminescence and scintillation characteristics were measured and mutually compared to further optimize the former compositions and reveal the reason for their lower scintillation performance with respect to GGAG:Ce. Correlated experiments of time-resolved luminescence and scintillation spectroscopies further completed by thermoluminescence glow curve measurement and electron paramagnetic resonance (performed on Gd-free Sc-admixed garnets) indicate that Sc^{3+} is situated at the dodecahedral site of the garnet lattice as a dominant electron trap, creating a bottleneck in the scintillation mechanism of Sc-admixed garnets. This is mainly responsible for the degradation of scintillation efficiency in comparison with GGAG:Ce despite nearly the same effects of Sc and Ga in lowering the conduction band edge in these multicomponent garnets. Calculations of the electronic band structure confirm that the 3d energy levels of Sc^{3+} at the dodecahedral site are situated in the forbidden gap in Sc-admixed garnets.

1. Introduction

Single-crystal multicomponent garnet scintillators of the general formula $(Gd,Y,Lu)_3(Al,Ga)_5O_{12}$:Ce were introduced in 2011,[1,2] and Czochralski-grown crystals with the composition $Gd_3Ga_xAl_{5-x}O_{12}$:Ce (x = 2.0–3.0), abbreviated as GGAG:Ce, reached the highest light yield of 58 000 ph MeV^{-1} (x = 2.7) or best energy resolution of 4.2%@662 keV (x = 2.4).[3] Luminescence and scintillation mechanisms, charge traps and different technological preparations have been studied in many laboratories worldwide.[4–16] In analogy to simple YAG:Ce and LuAG:Ce garnets, in GGAG:Ce, Mg^{2+} and Ca^{2+} codoping was used to accelerate the scintillation response owing to the stabilization of Ce^{4+} at the expense of reduction of light yield.[17–20] Despite such extended experimental efforts, electronic band structure calculations were absent for a long time and the first report appeared very recently,[21] confirming that the down energy shift of the conduction band (CB) edge is mainly due to the Ga energy levels.

Despite its excellent scintillation performance, a GGAG-based single-crystal scintillator poses a problem from the viewpoint of production economy. Large crystals can be grown only using the Czochralski technique with a very expensive iridium crucible. This is because the presence of gallium excludes the use of a reduction atmosphere and cheaper molybdenum or tungsten crucibles.[22,23] Thus, an alternative chemical composition was searched that provides a similar down energy shift of the CB bottom edge while enabling the use of cheaper crucibles. One such alternative could be Sc-admixed garnet, for which electronic band structure calculations have shown a substantial down energy shift of the CB bottom;[24] moreover, it has been shown that the addition of an admixture of Sc into GGAG:Ce slightly decreases the ionization barrier for Ce^{3+} $5d_1$ state quenching.[25] Kaurova *et al.*[26] determined that the crystal growth *via* the Czochralski technique from the initial melt composition of $Gd_3Sc_2Al_3O_{12}$ results in a crystal composition of $\{Gd_{2.69}Sc_{0.31}\}\{Sc_{1.93}Gd_{0.07}\}Al_3O_{12}$, *i.e.*, with pronounced occupation of the dodecahedral site by Sc and a minor occupation of the octahedral site by the Gd cation. The congruent composition for melt growth was determined to be $Gd_{2.88}Sc_{1.89}Al_{3.23}O_{12}$. Recently, the micropulling down (μ-PD) method was employed to prepare crystals of the Ce-doped congruent melting composition of $Gd_{2.88}Sc_{1.89}Al_{3.23}O_{12}$,[27] and the Bridgman method was used to prepare crystals of the congruent and stoichiometric melt compositions,[28] both from a molybdenum crucible under a reduction atmosphere. Their scintillation characteristics were reported to reach a maximum light yield of about 10 000 ph MeV^{-1}, which is about four times lower than that of μ-PD down grown crystals of GGAG:Ce in ref. 1. Very recently, a

[a] *Institute of Physics of the Czech Academy of Sciences, Cukrovarnicka 10/112, Prague, 16200, Czech Republic. E-mail: nikl@fzu.cz*
[b] *University of Chemistry and Technology, Department of Inorganic Chemistry, Technická 5, Prague, 166 28, Czech Republic*

† Electronic supplementary information (ESI) available. See DOI: https://doi.org/10.1039/d5ma00095e

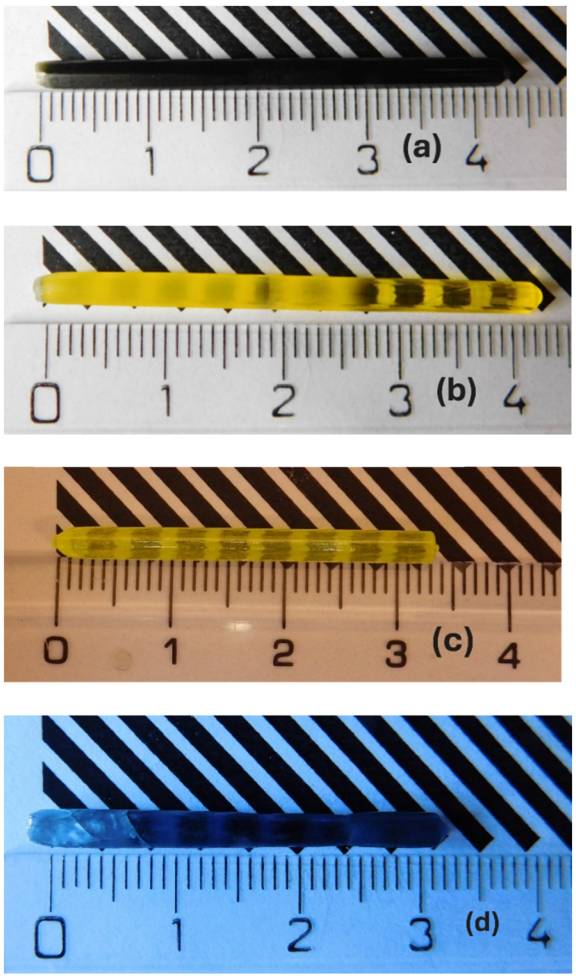

Fig. 1 Photographs of some of the grown crystals: (a) Gd_3Sc_2 as grown; (b) Gd_3Sc_2 air-annealed (1200 °C/12 h); (c) $Gd_3Ga_{2.7}$ as grown; and (d) $Y_3Sc_2Al_3O_{12}$ as grown.

substantial light yield increase of up to 15 000 ph MeV^{-1} was achieved in $Gd_3Sc_2Al_3O_{12}$:Ce (GSAG:Ce) crystals grown from a stoichiometric melt composition using the μ-PD method.[29]

This paper aims to search for further optimization of the scintillation characteristics of Gd-rich near-stoichiometric melt compositions of GSAG:Ce using the μ-PD crystal preparation method. By combining several optical and electron paramagnetic resonance (EPR) spectroscopies, we search for an explanation for its lower performance compared to that of the GGAG:Ce crystal prepared by applying the same technology. Furthermore, we perform quantum computation of the electronic band structure of various compositions of GSAG with different Sc concentrations to support the hypothesis of trapping migrating electrons in the transport stage of the scintillation mechanism derived from the experiment.

2. Experimental and calculation methods

2.1. Experimental methods

Crystals were grown by applying the μ-PD method; see the details in ref. 27 and 29 with radiofrequency inductive heating. The growth was performed using an Ir crucible with a die of 3 mm in diameter and a nozzle diameter of 0.5 mm under N_2(4N) + 1% O_2 atmosphere for the $Gd_3Ga_{2.7}Al_{2.3}O_{12}$:Ce crystal. The crucible was placed on an Ir afterheater with windows and an alumina pedestal. The hot zone around the crucible consisted of 3 layers of alumina shielding for thermal insulation. Other crystals were grown with a Mo crucible under an Ar + 5% H_2 reducing atmosphere to further verify a more economical method of crystal growth from the melt.[27–29] The gas flow was always kept at 0.5 L min^{-1}. The pulling speed was 0.3 mm min^{-1}. From crystal rods (see Fig. 1), plates of about 1 mm thick were cut and polished. Their chemical analysis was performed using the electron microanalyzer Jeol JX-8230 with energy-dispersive spectrometer Bruker QUANTAX 200 and using Esprit 2.2 software.

Measurement of absorption spectra within 200–800 nm was performed by applying the UV/VIS/NIR spectrometer, Shimadzu 3101PC. The photoluminescence (PL) excitation (PLE) and emission spectra and PL decay curves were measured using custom-made spectrofluorometer 5000 M (Horiba Jobin Yvon) with excitation sources: (i) steady-state laser-driven xenon lamp (PL and PLE spectra, Energetiq EQ-99X LDLS–A Hamamatsu company) and (ii) nanosecond nanoLED pulsed light sources (IBH Scotland, fast PL decays). The detection part of 5000 M consists of a single-grating monochromator and photon counting detector TBX04 (IBH Scotland). The measured spectra were corrected for the spectral dependence of excitation energy (PLE) and the spectral dependence of detection sensitivity (PL). A convolution procedure was applied to the decay curves to determine true decay times using the SpectraSolve software package (Ames Photonics).

Radioluminescence (RL) spectra and afterglow were measured on 5000 M using an X-ray tube with a Mo anode (40 kV, 15 mA, Seifert GmbH) as an excitation source. Thermoluminescence (TSL) glow curves were measured at 5000 M in the range of 77–500 K using a Janis cryostat with a heating rate of 0. 1 K s^{-1} after excitation by applying the X-ray tube at 77 K. The scintillation light yield measurements were performed on the sample wrapped in reflective PTFE tape and optically coupled with silicon grease to a hybrid photomultiplier (HPMT) Photonis PP0475B with a built-in preamplifier. The excitation gamma source, radioisotope ^{137}Cs (662 keV) and the amplifier shaping time of 1 μs were used in the measurement of pulse-height spectra. Scintillation decay curves were measured using the same ^{137}Cs (662 keV) excitation and the Hamamatsu PMT U7600 and digital oscilloscope TDS3052 in the detection part. The convolution procedure was used similarly to that used for the PL decay evaluation.

The EPR spectra were measured using a commercial Bruker EMX plus spectrometer operating at the X-band (microwave frequency 9.25–9.5 GHz) within the temperature range of 10–290 K.

2.2. Electronic band structure calculations

They were performed using MedeA software[30] with the implemented program VASP for electronic structure calculations. All calculations were based on the density functional theory (DFT)

Table 1 Composition of each oxide component is provided in formula units. Samples were annealed at 1200 °C/12 h in air

Sample	Gd_2O_3	Sc_2O_3	Al_2O_3	Ce_2O_3
Gd_3Sc_2	3.001	1.987	3.002	0.010
$Gd_{3.03}Sc_2$	3.032	2.007	2.953	0.008
$Gd_{3.09}Sc_2$	3.073	2.076	2.843	0.008
$Gd_3Ga_{2.7}$	3.050	2.700 (Ga_2O_3)	2.200	0.008

using the generalized gradient approximation (GGA)[31] and the projector augmented wave (PAW)[32] method. Specific pseudopotentials were set, Gd for Gd^{3+} and Sc_sv for Sc^{3+}, as recommended by MedeA. In the self-consistent field method, the tetrahedron method with Blöchl corrections was used as the integration scheme over the first Brillouin zone. A typical k-mesh density of 0.25 $Å^{-3}$ was applied. Owing to the strong correlation, we used LSDA + U with U = 7 eV for Gd-4f.[33] The calculation was spin-polarized magnetic with a default planewave cutoff energy of 400 eV. As the initial atomic structure of $Gd_3Al_5O_{12}$, we used a file from the ICSD database with a collection code of 23849.[34] All other initial Sc-doped garnet structures were created by lowering symmetry from Ia-3d to Pcca and changing the relevant atomic sites to Sc so that the dopant was evenly distributed. In some cases, multiple configurations with the same Sc concentration were calculated, and only the structure with the lowest energy was used afterwards. Structural optimization was performed with the conjugate gradient update algorithm with a convergence of 0.03 eV $Å^{-1}$. We optimized all atomic sites and lattice parameters so that the Pcca symmetry and lattice parameters were retained. All optimizations converged after *circa* 15 iterations because the initial system was very close to the optimized state. For the optimized structures, we calculated the density of states, where only the tetrahedron method was applied.

3. Results and discussion

3.1. Crystal growth

Using micropulling down technology, the crystals with initial melt composition of $Gd_3Sc_2Al_3O_{12}$:Ce0.3 at% (further denoted as Gd_3Sc_2), $Gd_{3.03}Sc_2Al3O_{12}$:Ce0.3 at% (further denoted as $Gd_{3.03}Sc_2$) and $Gd_{3.09}Sc_2Al_3O_{12}$:Ce0.3 at% (further denoted as $Gd_{3.09}Sc_2$) were grown using a molybdenum crucible and Ar + H_2 reduction atmosphere. For comparison purposes, we grew $Gd_3Ga_{2.7}Al_{2.3}O_{12}$:Ce0.3 at% crystal (further denoted as $Gd_3Ga_{2.7}$) using the same technology but with an Ir crucible and N_2 + 1% O_2 atmosphere. Photographs of selected crystals are illustrated in Fig. 1, and the composition measured at the sample plates is in Table 1. Crystals grown from molybdenum crucible were annealed at 1200 °C/12 h in the air to remove their dark color due to unspecified color centres (see Fig. 1). To enable EPR measurements requiring Gd-free compositions, we grew isostructural Gd-free crystals with melt compositions of $Y_3Sc_2Al_3O_{12}$ and $Y_{2.89}Sc_{1.16}Al_{3.95}O_{12}$, see also Fig. 1. The Gd-free crystals showed cracks in the initial part owing to a non-optimized temperature profile beneath the crucible in the crystal growth process.

3.2. Absorption spectra

As depicted in Fig. 2, the absorption spectra of Gd_3Sc_2 and $Gd_3Ga_{2.7}$ samples are shown. Different relative amplitudes of 4f–5d_1 (440–450 nm), 4f–5d_2 (340 nm) and 4f–5$d_{3,4,5}$ (220–240 nm) are noticed when both samples are compared, while their positions are almost the same. Long wavelength shift of 4f–5d_1 absorption band by about 8 nm in Gd_3Sc_2 indicates a slightly enhanced crystal field at the dodecahedral site when the Ga cation is changed to the Sc one. As expected, the positions and amplitudes of the Gd^{3+} 4f–4f transitions at 275 nm and 305–312 nm are the same in both samples. Most importantly, the position of the host band edge onset around 210–215 nm is almost the same in both samples, which evidences very similar positioning of the conduction band bottom edge.

The absorption spectra of the $Gd_{3.03}Sc_2$ and $Gd_{3.09}Sc_2$ samples in Fig. S1 (ESI†) are closely similar to that of Gd_3Sc_2 in Fig. 2.

3.3. Radioluminescence spectra

The RL spectra maxima of the Gd_3Sc_2, $Gd_{3.03}Sc_2$ and $Gd_{3.09}Sc_2$ samples (cca 550 nm) have long wavelength shifted with respect to the $Gd_3Ga_{2.7}$ one (530 nm), as illustrated in Fig. 3, which is consistent with the 4f–5d_1 band shift in the absorption spectra depicted in Fig. 2. The RL amplitudes of the Gd_3Sc_2, $Gd_{3.03}Sc_2$ and $Gd_{3.09}Sc_2$ samples are similar, about 2.5 times that of BGO, while that of $Gd_3Ga_{2.7}$ is much higher, about 8.3 times that of BGO, which indicates a much higher scintillation efficiency of the $Gd_3Ga_{2.7}$ sample.

3.4. Scintillation decays and afterglow

The scintillation decay of the Gd_3Sc_2 sample in Fig. 4 shows an even faster dominant decay component with a decay time of 90.1 ns 90.1 ns compared to the 111 ns of the $Gd_3Ga_{2.7}$, but its timing performance measured by the 1/e decay time (DT) is degraded by the presence of an intense rise component with a rise time of 70.6 ns. Even longer 1/e DT's is obtained for $Gd_{3.03}Sc_2$ (274 ns) and $Gd_{3.09}Sc_2$ (266 ns) samples (see Fig. S2a

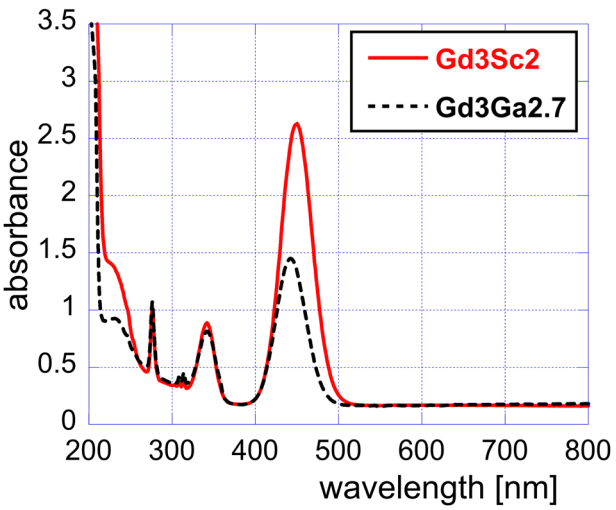

Fig. 2 Absorption spectra of Gd_3Sc_2 and $Gd_3Ga_{2.7}$ samples annealed at 1200 °C for 12 hours in air.

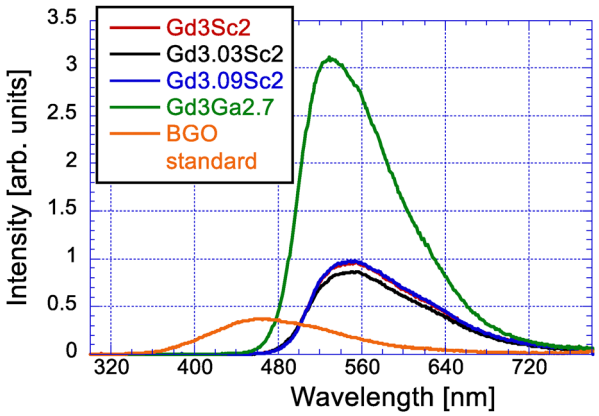

Fig. 3 RL spectra of the sample set in absolute comparison with the BGO standard scintillator.

and b (ESI†) and Table 2). Such intensely rising components were also evidenced in GSAG:Ce crystals prepared by applying the Bridgman method.[28]

The afterglow of all the samples in Fig. 5 is very competitive, within 0.02–0.03% at 10 ms after the X-ray cut-off, and that of the BGO standard is about 0.01%.

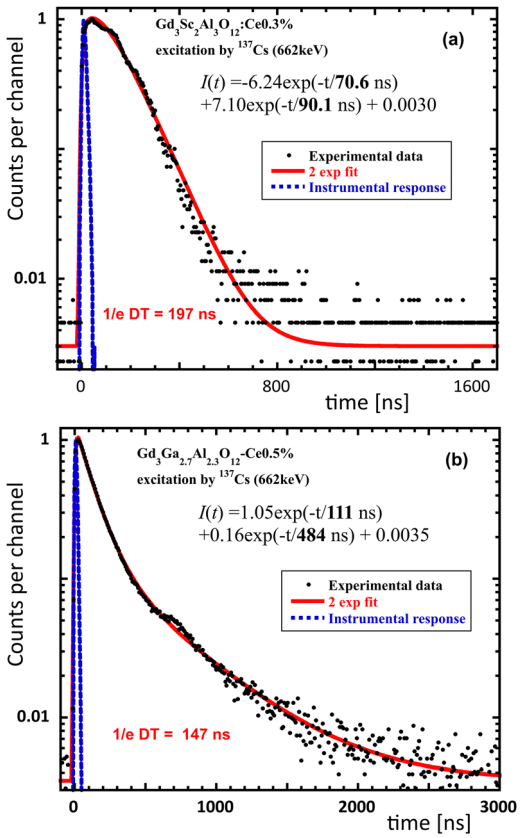

Fig. 4 Scintillation decays of (a) Gd_3Sc_2 and (b) $Gd_3Ga_{2.7}$, spectrally unresolved. The red line is the convolution of the instrumental response and function $I(t)$ in the figure.

Table 2 Summary of LY values and 1/e decay times for the sample set and the BGO standard sample. Excitation by ^{137}Cs (662 keV) and a shaping time of 1 μs. The errors of the LY and 1/e decay time values are within 5% and 1%, respectively

Sample	LY (ph MeV^{-1}) annealed 1200 °C	LY (ph MeV^{-1}) annealed 1200 & 1500 °C	1/e decay time (ns)
Gd_3Sc_2	15 080	16 810	197
$Gd_{3.03}Sc_2$	15 060	17 320	274
$Gd_{3.09}Sc_2$	14 030	15 360	266
$Gd_3Ga_{2.7}$	42 760	n/a	147
BGO standard	7850 (no annealing)	n/a	n/a

3.5. Photoluminescence decays

To determine the influence of the deteriorating processes of any kind acting at the excited state of the Ce^{3+} luminescence center at room temperature, PL decays are the best probe. As illustrated in Fig. 6, the PL decays of Gd_3Sc_2 and $Gd_3Ga_{2.7}$ are shown for direct comparison. The PL decays of $Gd_{3.03}Sc_2$ and $Gd_{3.09}Sc_2$ are very similar to that of Gd_3Sc_2, as shown in Fig. S3a and b (ESI†).

Considering the low temperature lifetimes of the 530 nm band in GGAG:Ce[1] and the 550 nm band in GSAG:Ce[27] around 55–60 ns and 65 ns, respectively, and the significantly faster decay of the Gd_3Sc_2 sample depicted in Fig. 6b, it can be concluded that the Ce^{3+} center in Gd_3Sc_2 is significantly quenched compared to the $Gd_3Ga_{2.7}$ host. The PLQY at RT, estimated from the mentioned decay times in the Gd_3Sc_2 sample, is about 49/65 = 0.75. The quenching process is due to the $5d_1$ excited state ionization.[1,27] However, the difference in the range of a few tens of percent cannot explain the huge difference in scintillation efficiency derived from the RL spectra depicted in Fig. 3. It is also worth noting that the PL decays are faster compared to the scintillation ones in Fig. 4 and Fig. S2a and b (ESI†), indicating additional delay/slowdown in the transfer stage of the scintillation mechanism.

3.6. Scintillation light yield

Scintillation light yield (LY) was measured with a 1 μs shaping time so that only fast enough scintillation light generated

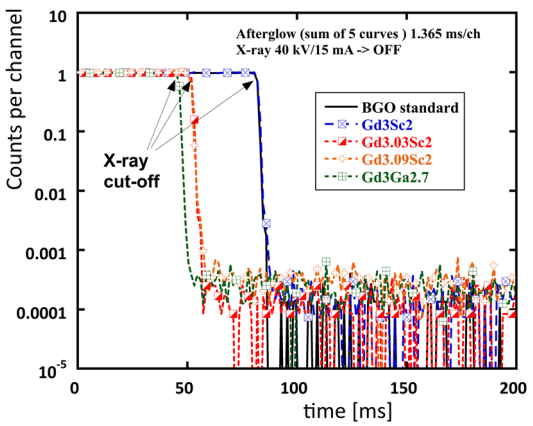

Fig. 5 Afterglow of all samples and the BGO standard. Curves are horizontally shifted for clarity, and the X-ray cut-off is indicated.

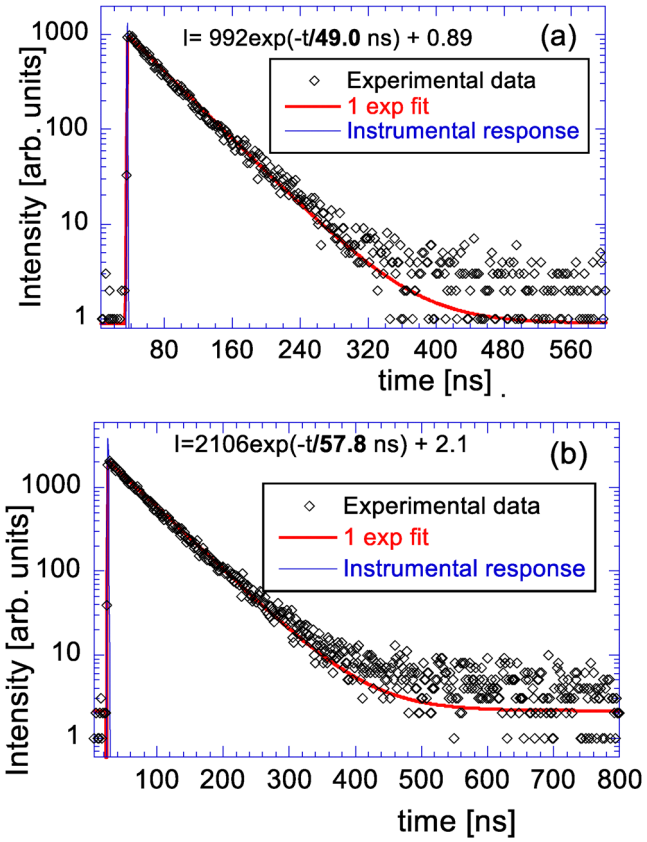

Fig. 6 PL decays at RT of (a) Gd_3Sc_2 and (b) $Gd_3Ga_{2.7}$ samples. Exc = 452 nm, Em = 550 nm (a) and 530 nm (b). The red solid line is the convolution of the instrumental response and the function $I(t)$ in the figure.

within this time window is registered here. As illustrated in Table 2, the values are summarized in ph MeV^{-1} units. Furthermore, the 2nd annealing in the air at 1500 °C/12 h was applied, which has shown a clear positive effect on all the Gd_3Sc_2, $Gd_{3.03}Sc_2$ and $Gd_{3.09}Sc_2$ samples. We applied yet another 3rd annealing at 1550 °C/12 h, which did not show any effect.

From all the data presented in Section 3.2–3.6, it can be observed that despite the similar decrease in CB bottom edge due to the Ga or Sc admixture in the garnet composition, which should deactivate some parts of the electron traps, the scintillation efficiency and the light yield are considerably lower in all the Sc-containing garnets compared to $Gd_3Ga_{2.7}$ prepared by applying the same μ-PD method. Somewhat more severe quenching observed in PL decays of Sc-containing garnets cannot explain such a huge difference, so the reason must involve a different mechanism of charge capture and nonradiative recombination processes in materials with Sc or Ga cations. This is discussed in Section 3.7.

3.7. Electron traps in Sc-containing garnets

In the Ce^{3+}-doped scintillators, most holes generated in the conversion stage of the scintillation mechanism are immediately and effectively captured by the Ce^{3+} ions owing to their high concentration and high ability for hole capture, becoming

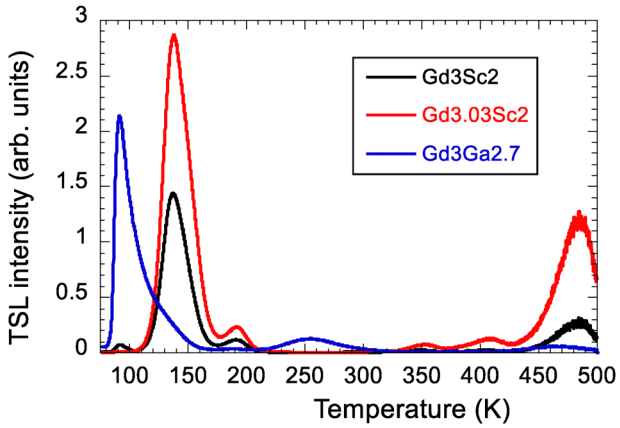

Fig. 7 TSL glow curves of selected samples corrected for the temperature dependence of PL spectra.

temporarily Ce^{4+}. The electrons, however, can be captured during the transfer stage of the scintillation mechanism at various electron traps, which delays their transport towards temporary Ce^{4+} to radiatively recombine here and yield scintillation photons. Thus, the study of electron traps in Ce-doped scintillation materials is of the utmost importance in revealing eventual bottlenecks and the limits of their performance.[35]

For the study of charge carrier capture in the lattice, the TSL and EPR experiments can be effectively correlated to reveal the acting traps and understand their nature. In Gd-based compounds, however, EPR cannot be used as a superstrong EPR signal from paramagnetic Gd^{3+} obscures signals from any other centers. Moreover, spins from any defect are exchange-coupled to Gd^{3+} spins, creating a very non-informative broad EPR signal. Thus, we prepared structurally equivalent $Y_3Sc_2Al_3O_{12}$ and $Y_{2.89}Sc_{1.16}Al_{3.95}O_{12}$ single crystals for the EPR study of electron traps.

3.7.1. Thermally stimulated luminescence measurement. The TSL glow curves depicted in Fig. 7 were corrected for quantum efficiency of the Ce^{3+} emission center using the temperature dependence of the integral of PL spectra; see Fig. S3 and S4 (ESI†) for the Gd_3Sc_2 and $Gd_3Ga_{2.7}$ samples, respectively. The TSL pattern of the Gd_3Sc_2 and $Gd_{3.03}Sc_2$ samples in Fig. 7 is very similar to that of the peak positions and shows a rich structure with intense glow peaks towards the highest temperatures, indicating the presence of deep electron traps in the material. The $Gd_3Ga_{2.7}$ sample shows the dominant peak at a lower temperature compared with the other two samples, and above room temperature, there is a nearly negligible TSL signal, which is consistent with the difference in LY values, as the deepest traps are usually responsible for LY loss in scintillation materials.[36] The lowest TSL signal in the range of 250–350 K illustrated in Fig. 7 in the Gd_3Sc_2 and $Gd_{3.03}Sc_2$ samples correlates with a lower intensity of afterglow in Fig. 5 within tens of ms after the X-ray cut-off compared with the $Gd_3Ga_{2.7}$ sample, which shows higher TSL intensity in this region and a somewhat higher level of afterglow as well.

3.7.2. Optical and EPR spectroscopy of $Y_3Sc_2Al_3O_{12}$ and $Y_{2.89}Sc_{1.16}Al_{3.95}O_{12}$ crystals. In the absorption spectrum of the as-grown sample shown in Fig. 8, there is a broad absorption band in the range of 600–900 nm, which is identical with the

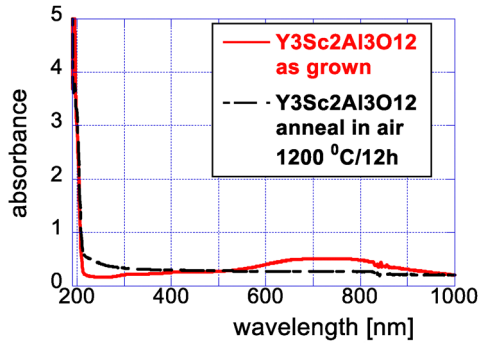

Fig. 8 Absorption spectra of $Y_3Sc_2Al_3O_{12}$ as grown and annealed in air at 1200 °C/12 h.

band observed in the undoped GSAG crystal ascribed to Sc^{2+} (or complex defect containing Sc^{2+}). It is destroyed after annealing at 1200 °C/3 h in the air accompanied by an increase in absorption below 400 nm, which could be due to unidentified hole centers.[37]

The EPR experiment confirmed the presence of defects containing Sc^{2+} ions in the as-grown crystal (Fig. 9, panel a). The spectrum in the as-grown sample is nearly isotropic (it is almost the same in the crystal and in the ground crystal) and is described by a *g*-factor of 1.980. It also shows a well-resolved hyperfine (HF) structure with eight equidistant lines that clearly originate from the ^{45}Sc isotope (nuclear spin I = 7/2, natural abundance = 100%, and hyperfine splitting $A = 54 \times 10^{-4}$ cm^{-1}). Annealing the crystal in the air leads to the disappearance of the Sc^{2+} spectrum (Fig. 9, panel b). These facts indicate that the center is of an F^+-type (an electron trapped at an oxygen vacancy), as observed previously in YAG[38] and LuAG crystals.[39] In contrast

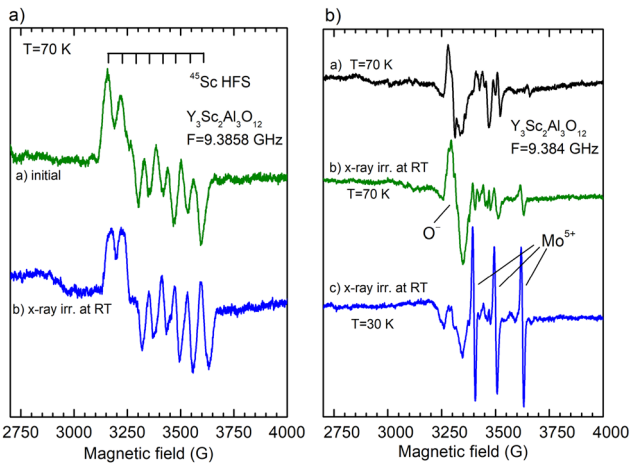

Fig. 9 Panel (a): EPR spectra in the $Y_3Sc_2Al_3O_{12}$ as-grown crystal; panel (b): EPR spectra in the $Y_3Sc_2Al_3O_{12}$ crystal annealed in air. Panel (a) presents EPR spectra measured in the crystal before X-ray irradiation (a) and in the crystal after X-ray irradiation at room temperature (b). The as-grown crystal shows an HF structure from the ^{45}Sc isotope (eight equidistant lines). Panel (b) presents EPR spectra measured in the crystal annealed in the air before X-ray irradiation (a) and after X-ray irradiation (b and c). In the annealed crystal, the spectrum with the ^{45}Sc HF structure is absent. Instead, the spectra of the O^- center and Mo^{5+} ions appear.

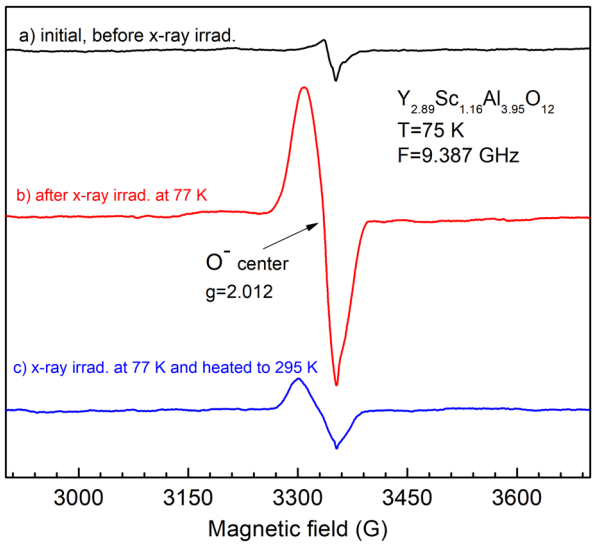

Fig. 10 O^- EPR spectrum measured in the X-ray irradiated (at 77 K) grinded $Y_{2.89}Sc_{1.16}Al_{3.95}O_{12}$ crystal. All spectra are measured at 75 K.

to the F^+ center in YAG or LuAG, an electron in the $Y_2Sc_2Al_3O_{12}$ is trapped at an oxygen vacancy in the vicinity of the Sc ion, as the electron density is markedly localized at the Sc ion (it follows from the observed hyperfine interaction with the ^{45}Sc nuclear spin). The center can thus be designed for the Sc^{2+}-V_O center. All these experimental facts suggest that the coloration of the as-grown $Y_3Sc_2Al_3O_{12}$ crystal is surely related to the presence of Sc^{2+}-V_O centers, which is consistent with the conclusion made in ref. 37 for the undoped GSAG crystal.

X-ray irradiation of the as-grown crystal does not create any additional EPR-active defects (Fig. 9, panel a, spectrum b). In contrast, the X-ray irradiation of air-annealed crystal creates O^- paramagnetic centers (Fig. 9, panel b, spectrum b). This is the most common defect created by X-ray or γ-ray irradiation in garnet crystals.[38] The O^- EPR spectrum is unusually strong in intensity in the $Y_{2.89}Sc_{1.16}Al_{3.95}O_{12}$ melt composition (Fig. 10), suggesting that O^- centers can be created in the vicinity of Sc ions at antisite position by trapping a hole by an oxygen lattice ion (such Sc ion makes strong perturbation for host oxygen ion, thus increasing the thermal stability of the O^- center). Besides, the EPR spectrum of Mo^{5+} ions appears as well (Fig. 9, panel b, spectrum c). The Mo ions come from the Mo crucible and, under irradiation, recharge to the Mo^{5+} valence state to compensate for (together with O^- ions) the excess negative charge in the lattice introduced by annealing in the air. Their concentration is estimated in the range of 0.1–1 at. ppm.

4. Electronic band structure calculations

Following,[26] we worked with the assumption that Sc can occupy only the octahedral and dodecahedral sites. We proposed and optimized superstructures with six different concentrations of evenly distributed Sc atoms on the octahedral and dodecahedral

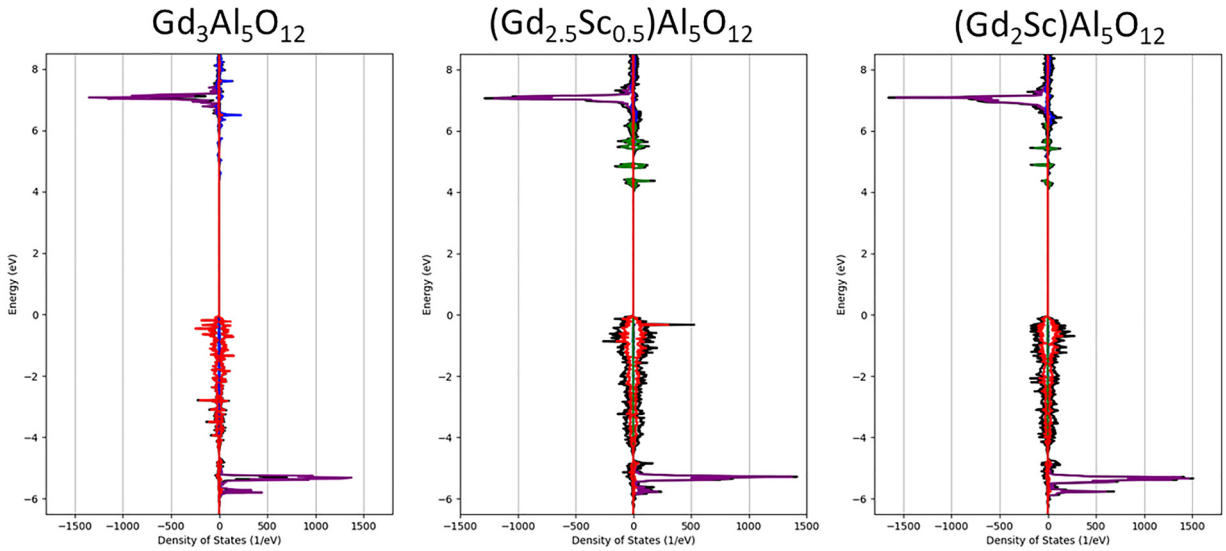

Fig. 11 Density of states of structures without Sc in the octahedral site. Total DOS is black, Gd-4f is purple, Gd-5d is blue, Sc-3d on the dodecahedral site is green and O-2p is red.

sites in $Gd_3Al_5O_{12}$ (GAG). With the optimized structures, we calculated the density of states and compared the energies of the bands, revealing primarily the character of the Sc valence states.

As depicted in Fig. 11 and 12, the density of states plots are presented, focusing on the valence and conduction bands. Partial DOS (PDOS) projected on the respective valence states of elements was multiplied by the number of equivalent Wyckoff positions to obtain the total PDOS per formula unit, *i.e.* for all equivalent atoms.

By calculating the DOS of the optimized structures of these Sc-admixed garnets, our results support the hypothesis drawn from the experiments, which demonstrates that the energies of the Sc^{3+}-3d states in dodecahedral sites are located in the bandgap under the conduction band minimum, creating electron traps. The shift of the Sc-3d levels deeper into the gap is imposed by weaker covalent bonding, making the Sc-3d orbitals less antibonding due to weaker metal–ligand orbital overlap, despite a slightly stronger crystal field of the dodecahedral position with a higher coordination number.

5. Conclusions

Using micropulling down technology, single crystals of the starting melt composition $Gd_3Sc_2Al_3O_{12}$:Ce0.3 at%, $Gd_{3.03}Sc_2Al_3O_{12}$:Ce0.3 at%, and $Gd_{3.09}Sc_2Al_3O_{12}$:Ce0.3 at% were grown from a molybdenum crucible under a reduction atmosphere and $Gd_3Ga_{2.7}Al_{2.3}O_{12}$:Ce0.3 at% crystal from an Ir crucible

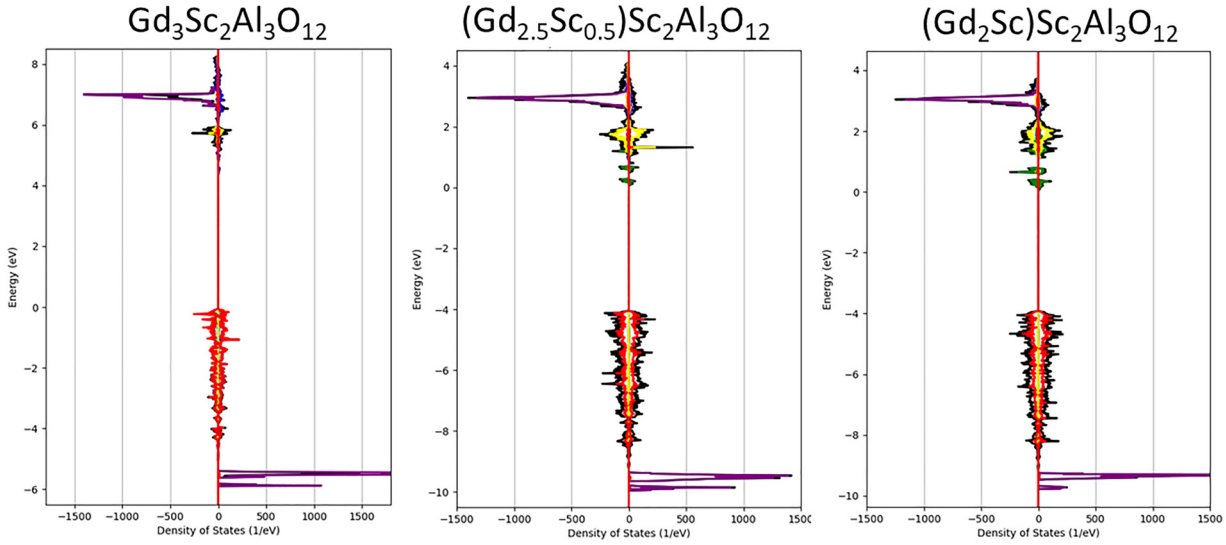

Fig. 12 Density of states of structures with Sc in both the octahedral and dodecahedral sites. Total DOS is black, Gd-4f is purple, Gd-5d is blue, Sc-3d on the dodecahedral site is green, Sc-3d on the octahedral site is yellow and O-2p is red. The Gd-5d band is hidden under the Sc-3d line.

under N_2 + 1%O_2 atmosphere. Crystal compositions were determined by applying an electron microprobe method. Annealing in the air at 1200 °C/12 h and 1500 ^{0}C/12 h was applied to the former group in two steps. The optical, luminescence and scintillation characteristics were measured for all of them to compare characteristics between the Sc-admixed and Ga-admixed crystals. The highest light yield was obtained in the doubly air annealed $Gd_{3.03}Sc_2Al_3O_{12}$:Ce0.3 at% crystals, providing a value of 17 320 ph MeV^{-1}, while that of $Gd_3Ga_{2.7}Al_{2.3}O_{12}$:Ce0.3% was 42 760 ph MeV^{-1}. Similarly, the amplitudes of their RL spectra compared to BGO were about 2.5 and 8.3, respectively. Furthermore, the $Y_3Sc_2Al_3O_{12}$ and $Y_{2.89}Sc_{1.16}Al_{3.95}O_{12}$ crystals were grown similarly to the Sc-admixed Gd-based ones and used for the EPR experiment to determine the nature of the electron traps. Electronic band structure calculations were performed for several compositions of the Sc-admixed garnet structure.

The significantly lower scintillation performance of the Sc-admixed garnets compared with the well-established $Gd_3Ga_{2.7}Al_{2.3}O_{12}$:Ce0.3 at% multicomponent garnets is explained by the antisite Sc^{3+} ion at the dodecahedral position of $Gd^{3+}(Sc_{Gd})$ in the garnet structure, which forms a deep electron trap. Electron capture at Sc^{3+} was proved by EPR, creating the Sc^{2+}-V_O center in the as-grown $Y_3Sc_2Al_3O_{12}$ crystal, which is also responsible for absorption bands in the range of 600–900 nm. This center and its related absorption disappear after annealing in air at 1200 °C/12 h. An anomalously high concentration of O^- centers is revealed in $Y_{2.89}Sc_{1.16}Al_{3.95}O_{12}$ annealed in air at 1200 °C/12 h by EPR compared to $Y_3Al_5O_{12}$ or $Lu_3Al_5O_{12}$ crystals. Such centers require charge compensation in the lattice, and the Sc^{2+} is the most probable option. Intense TSL glow curves above room temperature evidence the existence of deep electron traps in the Ce-doped Sc-admixed crystals, and the electronic band structure calculations show that the Sc^{3+} at the dodecahedral position forms the energy levels within the forbidden gap below the bottom of the conduction band, which provides further support for such an explanation.

Thus, despite a similar downshift of conduction band bottom edge in the $Gd_3Sc_2Al_3O_{12}$ and $Gd_3Ga_{2.7}Al_{2.3}O_{12}$ structures, which should deactivate shallow electron traps, such a new deep electron trap in the Sc-admixed garnets, the formation of which is an intrinsic feature in the crystal grown from the melt, significantly deteriorates its scintillation performance for the overall scintillation efficiency and light yield characteristics.

Author contributions

Martin Nikl: conceptualization, data curation, investigation, validation, visualization, writing – original draft, writing – review & editing, funding acquisition, supervision. Jan Pejchal: crystal growth, writing – review & editing. Jakub Ježek and David Sedmidubský: theoretical calculations, writing – original draft, writing – review & editing. Kučerková Romana: data curation, formal analysis, investigation, visualization. Valentin Laguta: EPR experiment, data curation, formal analysis, investigation, visualization, writing – original draft writing – review & editing. Vladimir Babin: TSL experiment, data curation, formal analysis, investigation, visualization, writing – review & editing. Alena Beitlerová, Romana Kučerková: data curation, formal analysis, investigation.

Data availability

The data related to figures are available upon request from the corresponding author.

Conflicts of interest

There are no conflicts of interest to declare.

Acknowledgements

This research was supported by Czech Science Foundation project no. 21-17731S and by OP JAC financed by ESIF and MEYS (project LASCIMAT–CZ.02.01.01/00/23_020/0008525). Computational resources were provided by the e-INFRA CZ project (project ID no.: 90254), supported by the Ministry of Education, Youth and Sports of the Czech Republic. We acknowledge the help of K. Jurek and M. Jarošová, who performed chemical analysis of the samples.

References

1 K. Kamada, T. Yanagida, T. Endo, K. Tsutumi, Y. Fujimoto, A. Fukabori, A. Yoshikawa, J. Pejchal and M. Nikl, *Cryst. Growth Des.*, 2011, **11**, 4484–4490.
2 K. Kamada, T. Yanagida, J. Pejchal, M. Nikl, T. Endo, K. Tsutumi, Y. Fujimoto, A. Fukabori and A. Yoshikawa, *J. Phys. D: Appl. Phys.*, 2011, **44**, 505104.
3 K. Kamada, S. Kurosawa, P. Prusa, M. Nikl, V. V. Kochurikhin, T. Endo, K. Tsutumi, H. Sato, Y. Yokota, K. Sugiyama and A. Yoshikawa, *Opt. Mater.*, 2014, **36**, 1942–1945.
4 O. Sidletskiy, V. Kononets, K. Lebbou, S. Neicheva, O. Voloshina, V. Bondar, V. Baumer, K. Belikov, A. Gektin and B. Grinyov, *Mater. Res. Bull.*, 2012, **47**, 3249–3252.
5 P. Dorenbos, *J. Lumin.*, 2013, **134**, 310–318.
6 J. M. Ogiegło, A. Katelnikovas, A. Zych, T. Justel, A. Meijerink and C. R. Ronda, *J. Phys. Chem. A*, 2013, **117**, 2479–2484.
7 K. Brylew, W. Drozdowski, A. J. Wojtowicz, K. Kamada and A. Yoshikawa, *J. Lumin.*, 2014, **154**, 452–457.
8 V. Laguta, Y. Zorenko, V. Gorbenko, A. Iskaliyeva, Y. Zagorodniy, O. Sidletskiy, P. Bilski, A. Twardak and M. Nikl, *J. Phys. Chem. C*, 2016, **120**, 24400–24408.
9 I. I. Vrubel, R. G. Polozkov, I. A. Shelykh, V. M. Khanin, P. A. Rodnyi and C. R. Ronda, *Cryst. Growth Des.*, 2017, **17**, 1863–1869.
10 C. Wang, D. Ding, Y. Wu, H. Li, X. Chen, J. Shi, Q. Wang, L. Ye and G. Ren, *Appl. Phys. A*, 2017, **123**, 1–6.
11 M. Kitaura, H. Zen, K. Kamada, S. Kurosawa, S. Watanabe, A. Ohnishi and K. Hara, *Appl. Phys. Lett.*, 2018, **112**, 031112.

12 V. Kochurikhin, K. Kamada, K. J. Kim, M. Ivanov, L. Gushchina, Y. Shoji, M. Yoshino and A. Yoshikawa, *J. Cryst. Grow.*, 2020, **531**, 125384.
13 M. Li, M. Meng, J. Chen, Y. Sun, G. Cheng, L. Chen, S. Zhao, B. Wan, H. Feng, G. Ren and D. Ding, *Phys. Status Solidi B*, 2021, **258**, 2000603.
14 S. Nargelas, Y. Talochka, A. Vaitkevičius, G. Dosovitskiy, O. Buzanov, A. Vasil'ev, T. Malinauskas, M. Korzhik and G. Tamulaitis, *J. Lumin.*, 2022, **242**, 118590.
15 T. Wu, *et al.*, *Cryst. Growth Des.*, 2022, **22**, 180–190.
16 A. Yoshikawa, V. V. Kochurikhin, M. Yoshino, R. Murakami, T. Tomida, I. Takahashi, K. Kamada, Y. Shoji, H. Sato, R. Kucerkova, A. Beitlerova and M. Nikl, *Cryst. Growth Des.*, 2023, **23**, 2048–2054.
17 Y. Wu, F. Meng, Q. Li, M. Koschan and C. L. Melcher, *Phys. Rev. Appl.*, 2014, **2**, 044009.
18 K. Kamada, M. Nikl, S. Kurosawa, A. Beitlerova, A. Nagura, Y. Shoji, J. Pejchal, Y. Ohashi, Y. Yokota and A. Yoshikawa, *Opt. Mater.*, 2015, **41**, 63–66.
19 G. Tamulatis, G. Dosovitskiy, A. Gola, M. Korjik, A. Mazzi, S. Nargelas, P. Sokolov and A. Vaitkevičius, *J. Appl. Phys.*, 2018, **124**, 215907.
20 M. Korzhik, V. Alenkov, O. Buzanov, G. Dosovitskiy, A. Fedorov, D. Kozlov, V. Mechinsky, S. Nargelas, G. Tamulaitis and A. Vaitkevičius, *CrystEngComm*, 2020, **22**, 2502–2506.
21 F. Zajíc, V. Jarý, J. Pospíšil, P. Boháček, Z. Umar, M. Piasecki, M. G. Brik, R. Kučerková, A. Beitlerová and M. Nikl, *Mater. Adv.*, 2024, **6**, 777–787.
22 O. Sidletskiy, P. Arhipov, S. Tkachenko, Ia Gerasymov, D. Kurtsev, V. Jarý, R. Kučerková, M. Nikl, K. Lebbou and E. Auffray, Engineering of Scintillation Materials and Radiation Technologies, ISMART, in *Springer Proceedings in Physics*, ed. M. Korzhik, A. Gektin, 2018, vol. 227, Springer, Cham.
23 K. Kamada, *et al.*, *J. Cryst. Grow.*, 2020, **535**, 125510.
24 Y.-N. Xu, W. Y. Ching and B. K. Brickeen, *Phys. Rev. B: Condens. Matter Mater. Phys.*, 2000, **61**, 1817–1824.
25 D. Spassky, *et al.*, *CrystEngComm*, 2020, **22**, 2621–2631.
26 I. A. Kaurova, E. N. Domoroshchina, G. M. Kuz'micheva and V. B. Rybakov, *J. Cryst. Grow.*, 2017, **468**, 452–456.
27 O. Zapadlík, J. Pejchal, R. Kučerková, A. Beitlerová and M. Nikl, *Cryst. Growth Des.*, 2021, **21**, 7139–7149.
28 K. L. Hovhannesyan, M. V. Derdzyan, G. Badalyan, G. Kharatyan, J. Pejchal, M. Nikl, C. Dujardin and A. G. Petrosyan, *CrystEngComm*, 2024, **26**, 4812–4819.
29 O. Zapadlík, J. Pejchal, V. Babin, V. Jarý, V. Vaněček, R. Kučerková, K. Jurek, A. Beitlerová and M. Nikl, *RSC Adv.*, 2025, **15**, 2140–2151.
30 G. Kresse and J. Furthmüller, *Phys. Rev. B: Condens. Matter Mater. Phys.*, 1996, **54**, 11169–11186.
31 J. P. Perdew, K. Burke and M. Ernzerhof, *Phys. Rev. Lett.*, 1996, **77**, 3865.
32 G. Kresse and D. Joubert, *Phys. Rev. B: Condens. Matter Mater. Phys.*, 1999, **59**, 1758–1775.
33 L. Dudarev, S. Y. Savrasov, C. J. Humphreys and A. P. Sutton, *Phys. Rev. B: Condens. Matter Mater. Phys.*, 1998, **57**, 1505.
34 F. Euler and J. A. Bruce, *Acta Crystallogr.*, 1965, **19**, 971–978.
35 M. Nikl, V. V. Laguta and A. Vedda, *Phys. Status Solidi B*, 2008, **245**, 1701–1722.
36 F. Moretti, G. Patton, A. Belsky, M. Fasoli, A. Vedda, M. Trevisani, M. Bettinelli and C. Dujardin, *J. Phys. Chem. C*, 2014, **118**, 9670–9676.
37 K. L. Hovhannesyan, M. V. Derdzyan, I. A. Ghambaryan, T. I. Butaeva, C. Dujardin and A. G. Petrosyan, *Phys. Status Solidi A*, 2023, **220**, 2300386.
38 V. Laguta, M. Buryi, P. Arhipov, O. Sidletskiy, O. Laguta, M. G. Brik and M. Nikl, *Phys. Rev. B*, 2020, **101**, 024106.
39 V. Laguta, M. Buryi, J. Pejchal, V. Babin and M. Nikl, *Phys. Rev. Appl.*, 2018, **10**, 034058.